

# Chapter 3

## Elastic scattering and Fusion cross sections measurement for ${}^7\text{Li} + {}^{27}\text{Al}$ system

### 3.1 Introduction

Nuclear reaction dynamics that involves weakly bound or halo nuclei is a field of current interest because of its application to research in astrophysics, nuclear structure and production of super heavy elements [21, 54]. Due to lower breakup thresholds of loosely bound nuclei, the direct breakup channels become more probable during nuclear interactions that affects the elastic scattering and fusion cross sections at around the Coulomb barrier energies. In recent times, measurement of elastic scattering angular distributions and fusion cross sections have been found to be the main alternatives to reveal the breakup coupling phenomena. If any channel coupling effects are there then one can make observation on presence or absence of the ‘Threshold Anomaly (TA)’ by studying the energy dependences of the optical potential parameters. In case of weakly bound nuclei such as  ${}^6,7\text{Li}$ ,  ${}^9\text{Be}$ (breakup threshold energies ranging from 1.47 to 2.47 MeV), ‘Breakup Threshold Anomaly’ has been seen which is contrary to the case of tightly bound nuclei

as explained in the Sec.1.4 (See Chapter 1). The breakup or any other channels coupling may also affect the fusion cross sections by enhancing or suppressing its magnitudes. Thus, simultaneous measurement of elastic scattering angular distributions and fusion cross sections can provide a clear understanding of breakup channels coupling.

### 3.1.1 Present measurement

Simultaneous measurement of elastic scattering angular distributions and fusion cross sections have been carried out for  ${}^7\text{Li} + {}^{27}\text{Al}$  system in the energy range from below to above the Coulomb barrier energy ( $E_{lab} \sim 8.0 \text{ MeV} = V_b = 16.0 \text{ MeV}$ ). From the elastic scattering angular distributions energy dependence of the optical potential parameters have been carried out using Woods-Saxon form of potential. The fusion cross-sections have been obtained from the  $\alpha$ -evaporation energy spectra. To avoid any systematic errors in the normalization of the  $\alpha$ -energy spectrum to the elastic scattering at a particular angle and beam energy, it is of paramount importance that the data for the above channels are measured in the same experimental setup. The coupled-channels calculations are also performed to study the effect of direct reaction channels on elastic scattering and fusion cross-sections with the potential and coupling parameters constrained by the data from the present measurements as well as the data from the literature. The experiment was carried out at Folded Tandem Ion Accelerator (FOTIA) Facility (Sec:3.1.2) at BARC, Mumbai, India using  ${}^7\text{Li}$  beam.

### 3.1.2 Accelerator Facility

The Fig.3.1 shows schematic diagram of the 6 MV Folded Tandem Ion Accelerator (FOTIA) facility at Bhabha Atomic Research Centre, Mumbai, India. The FOTIA facility can deliver ion beams of mass up to 40, and energy up to 66 MeV (for a charge state of  $10^{(+)}$  and maximum terminal voltage of 6 MV)[55, 56].

In this facility, at the first stage, the negative ion beams extracted from the SNICS (Source of Negative Ions through Cesium Sputtering) source are pre-accelerated up to 150 keV. After that, out of all the charged particles extracted from the ion source the negative ions of the desired mass are selected using a  $70^\circ$ -dipole magnet for injection into the low energy accelerating tube through the  $20^\circ$  electrostatic deflector. In order to focus and match the beam parameters to the acceptance of the low energy tube, an electrostatic quadrupole triplet and an einzel lens are used. The electrons of these accelerated negative ions get stripped off at the stripper and leave positive ions. A particular charge state of the positive ions thus produced, is selected using  $180^\circ$  magnet inside the high voltage terminal (up to 6 MV). At this stage the produced beam diverges. So, at the exit of the  $180^\circ$  magnet the beam, an electrostatic quadrupole doublet is used to focus the beam before it enters the high-energy tube. Thus the desired beam is again accelerated through the high energy accelerating tube to the ground potential. At the exit of the high energy accelerating tube the beam is then focused by the magnetic quadrupole triplet, and then analyzed by the  $90^\circ$  bending magnet. The analyzed beam is guided to the scattering chamber through the experimental beam line that includes second magnetic quadrupole triplet and the switching magnet, magnetic steerer, Beam Profile Monitor (BPM), Faraday cups.

## 3.2 Experimental setup and Electronics

The schematic picture of the scattering chamber and the experimental setup is shown in the Fig.3.2. The targets were mounted inside the 80 cm diameter scattering chamber. The elastically scattered particles were detected in the angular range from forward to backward angles at various bombarding energies. For the identification of charged particles, the silicon surface barrier (SSB) detector telescopes were mounted on the rotating arms [3.2]. Fig.3.3 shows the picture of scattering chamber at FOTIA facility. Fig. 3.4 gives the schematic diagram of detector telescopes that have been used in the present experiment. Fig. 3.5 shows the

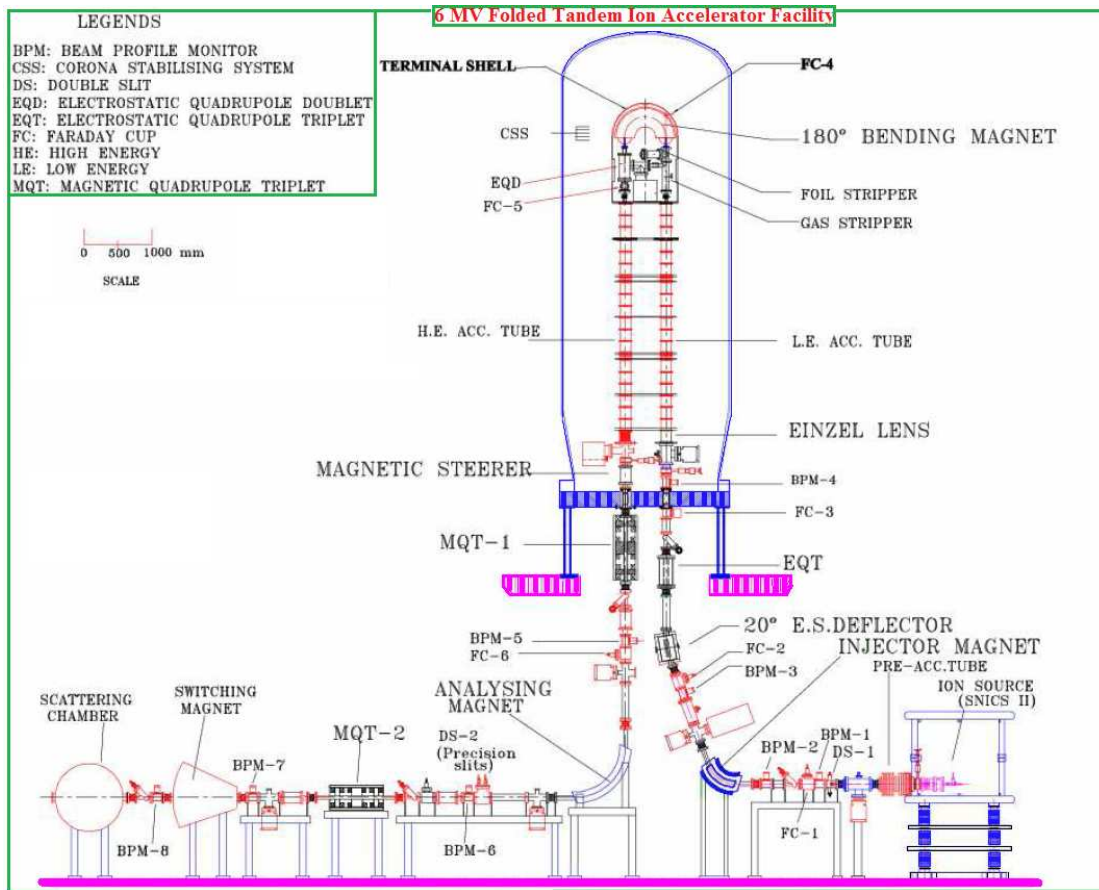


FIGURE 3.1: Schematic picture of FOTIA facility at NPD, BARC, Mumbai

schematic representation of the electronic setup in conjunction with the detector telescopes, used to acquire the data signals that come from the reaction.

Since the signals from the detectors have small amplitude, they must be amplified by using pre-amplifier(PA) putting it close to the detector. The slow output from the pre-amplifier are used to measure the energy deposited in the detector material. Thus, from each detector (concerned to each detector telescope), via coaxial cables, the signal is sent to the pre-amplifier(PA) which is followed by the amplifier(AMP). The signals drawn to the amplifier(AMP) are further amplified and shaped by the inbuilt  $RC$  and  $CR$  circuits in the amplifier. In order to have timing information output of the  $\Delta E$  detectors is chosen and a fast output (with a rapid rise time) from the preamplifier is sent to the Timing Filter Amplifier(TFA). The Timing Filter Amplifier(TFA) filters the signal from the pre-amplifier and also preserve the fast output pulse shape thereby not affecting the high frequency

components. The resulting outputs that are coming from all the  $\Delta E$  detectors are fed to the Constant Fraction Discriminator(CFD) with a long delay cable to get delayed output. This delayed output is used as stop signal and the corresponding start signal was taken from the main trigger for Time to Digital Converter(TDC). All the fast(timing) signals from the CFD, through the logic OR gate, are sent to the Gate and Delay Generator(GDG), where the main common gate is built and given as master strobe to the Analog to Digital Converter(ADC). ADC converts all the analog signal to the equivalent digital form, thus its a fundamental link between analog and digital electronics[57]. Then, with the help of BUS, the digital signals from ADC are sent to the the data acquisition system called ‘LAMPS’ [58]. ‘LAMPS’ (Linux Advanced Multi parameter system) is widely used for data acquisition and analysis. It can also be used for off line data analysis.

### 3.2.1 Identification of charged particles

In order to identify various charged fragments with respect to mass( $M$ ) and charge( $Z$ ) and the energy, a combination of two ( $\Delta E$  and  $E$ ) silicon surface barrier detectors were made. Detector telescopes were mounted on a movable arm to carry out angular measurements. The  $\Delta E$  detector is of smaller thickness as compared to the  $E$  detector[59]. In the  $\Delta E$  detector the particles lose some fraction of its total energy and the remaining in the  $E$  detector. Combining these two energies give total energy of the detected charged fragments. When charged particles interact with the detector material, the particular energy loss of charged particles by the well known Bethe-Bloch formula is given by,

$$\frac{dE}{dx} \propto \frac{Z^2}{v^2} \propto \frac{1}{E} \times MZ^2 \quad (3.1)$$

Where,  $z$ ,  $v$  and  $M$  are the charge, velocity and mass of the charge particle. The identification of different charged fragments using  $\Delta E + E$  configuration is based on this relation. The energy losses will be different for different charged particles at a given energy  $E$ . Thus, in the plot of  $\Delta E$  Vs  $E_{total}$ , different bands that corresponds to different mass( $M$ ) and charge( $Z$ ) are obtained. A schematic

picture of detector telescopes that contains  $\Delta E$  and  $E$  (*sb*) detectors is shown in Fig.3.4.

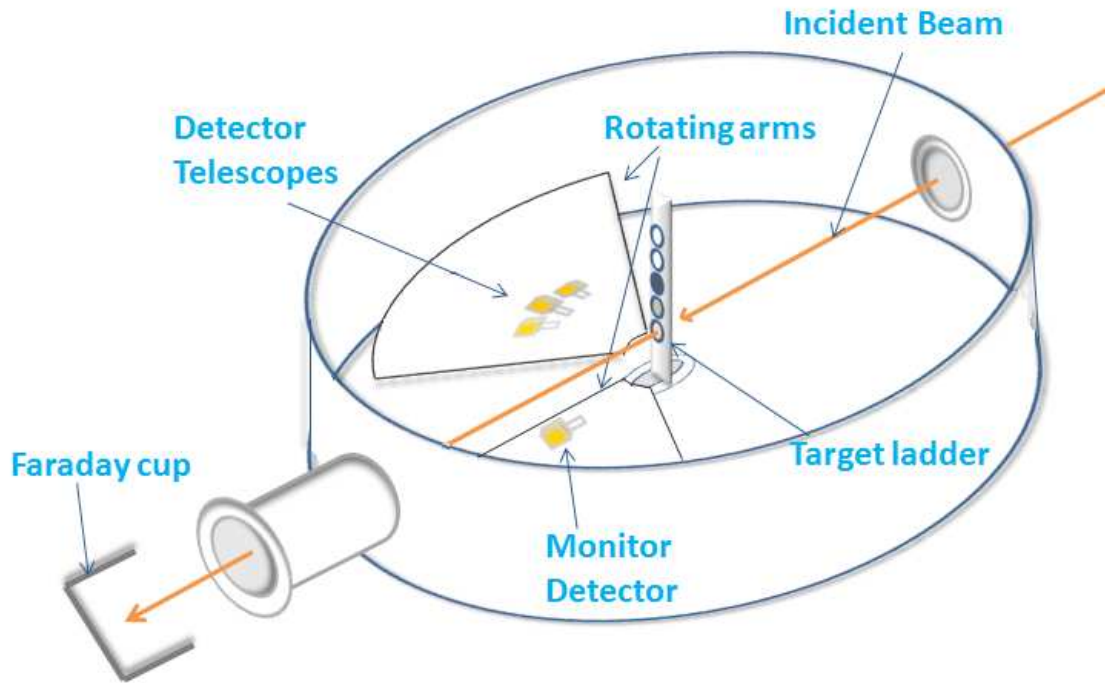


FIGURE 3.2: Schematic picture of scattering chamber and experimental setup

### 3.3 Experimental Details

The details of FOTIA facility has been given in the Sec.3.1.2. The elastic scattering and  $\alpha$ -particle angular distribution have been measured simultaneously in the same experimental setup at six different bombarding energies (8, 9, 10, 12, 14, and 16 MeV) for the  ${}^7\text{Li} + {}^{27}\text{Al}$  system. A self-supported  ${}^{27}\text{Al}$  target of thickness  $\sim 100 \mu\text{g}/\text{cm}^2$  was used, except for the measurement at 9 MeV beam energy where a target of  $\sim 220 \mu\text{g}/\text{cm}^2$  thickness was used. Also, a self-supported  ${}^{12}\text{C}$  target of  $\sim 50 \mu\text{g}/\text{cm}^2$  thickness was used for  $\alpha$ -particle energy calibration through  ${}^{12}\text{C}({}^7\text{Li}, \alpha){}^{15}\text{N}$  reaction. The energy calibration was done by using discrete groups of  $\alpha$ -particles with known energies produced in the above reaction.

The energy corrections were also done by calculating energy loss of the incident beam at the center of the target. In the measurements, three telescopes ( $\Delta E$  -

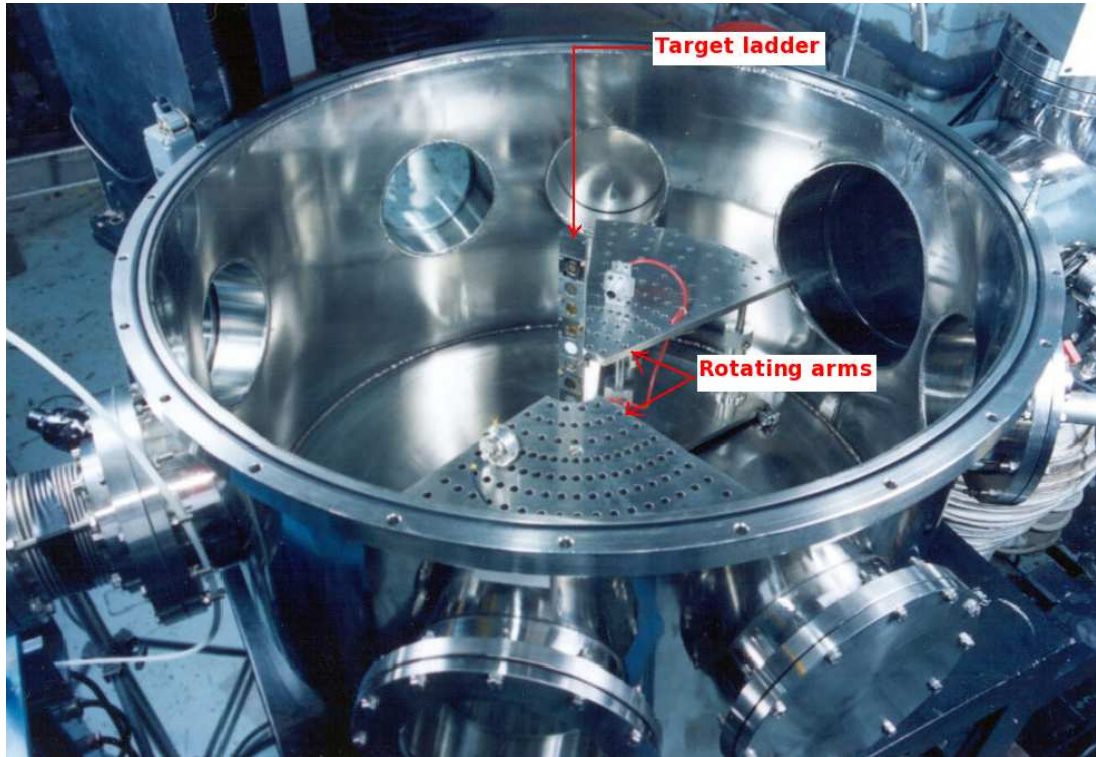


FIGURE 3.3: A picture of scattering chamber at FOTIA facility.

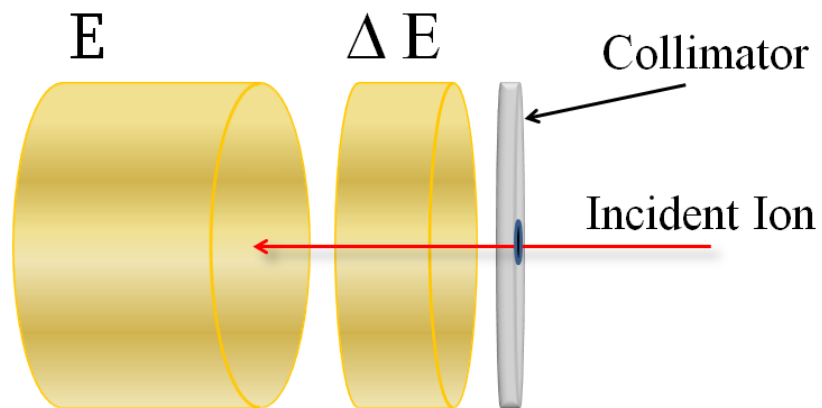


FIGURE 3.4: Schematic diagram of detector telescopes that contains  $\Delta E$  and  $E$  (*ssb*) detectors

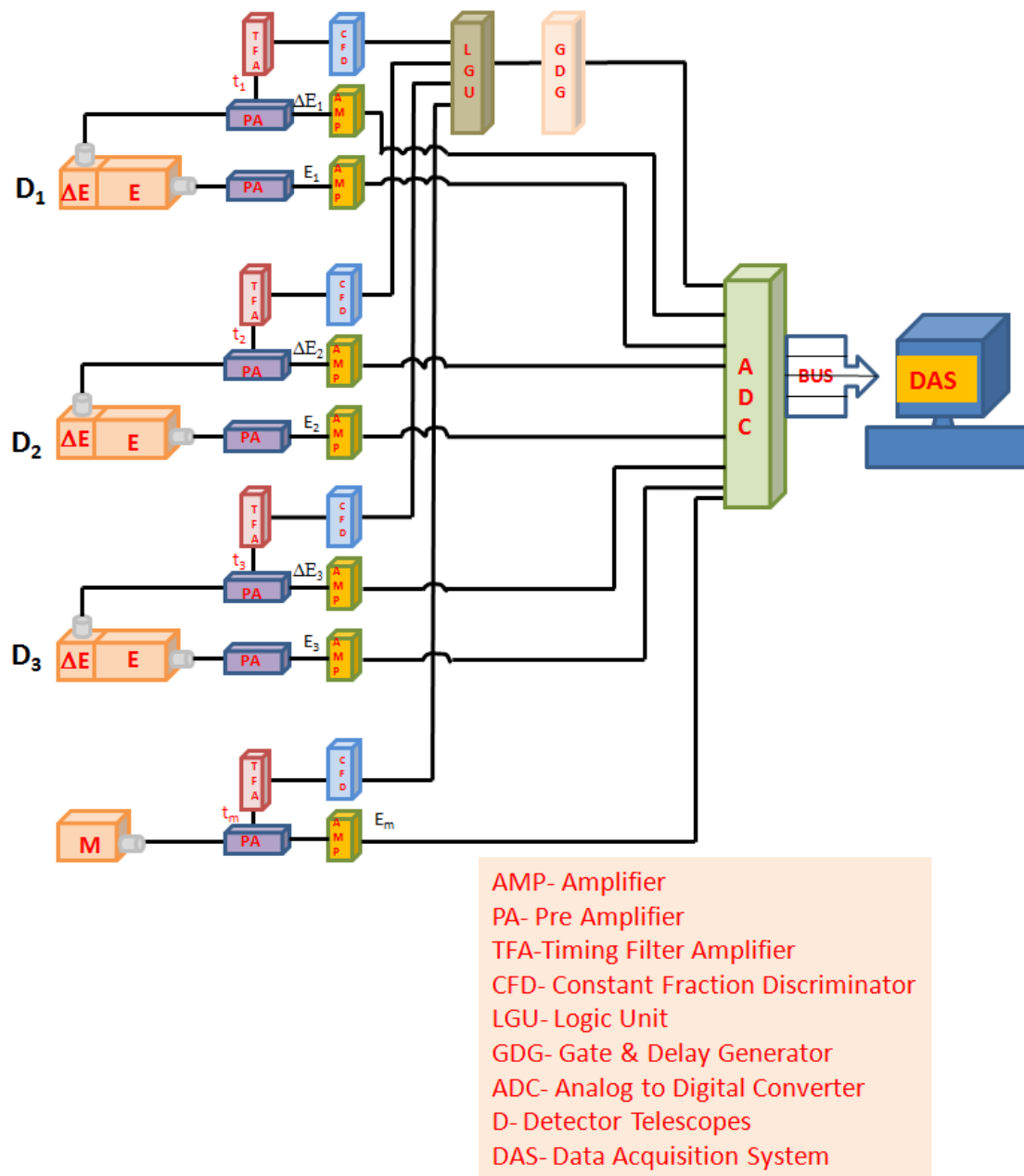


FIGURE 3.5: Block diagram of electronics associated with the detector telescopes

E) of silicon surface barrier detectors of thicknesses  $22 \mu\text{m} + 1.5 \text{ mm}$ ,  $17 \mu\text{m} + 1 \text{ mm}$  and  $15 \mu\text{m} + 300 \mu\text{m}$  respectively with a separation of  $10^\circ$  have been used. The solid angle subtended by each telescope was about  $0.5 \text{ msr}$ . A typical bi-parametric  $\Delta E$ - $E_{total}$  spectrum for the  ${}^7\text{Li} + {}^{27}\text{Al}$  system at  $E_{lab} = 9.0 \text{ MeV}$  and  $\theta_{lab} = 40^\circ$ , is shown in Fig.3.6. For the purpose of Rutherford normalization and to check the leftright beam wandering, two Silicon surface barrier detectors of  $300 \mu\text{m}$  thickness were kept at  $\pm 20^\circ$  with respect to the beam direction. The typical

beam current was  $\sim 10\text{-}15$  nA. The angular range for elastic scattering angular distributions was from  $10^\circ$  to  $160^\circ$ . For  $\alpha$ -particle energy spectra (that were used to obtain fusion cross-section) measurements were carried out in the angular range of  $110^\circ$  to  $150^\circ$ .

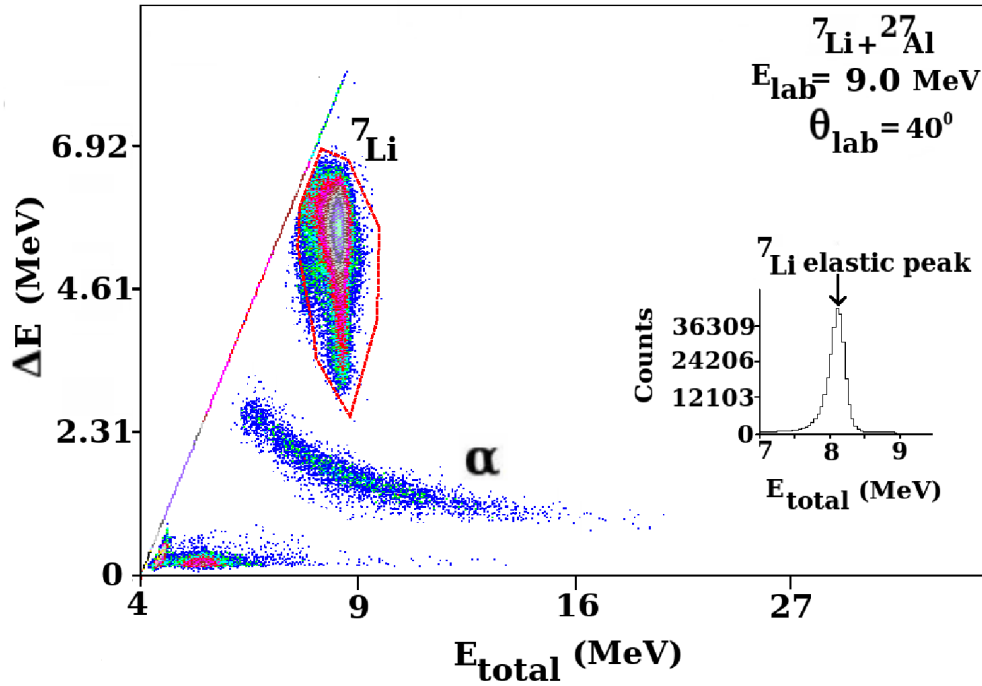


FIGURE 3.6: A typical two-dimensional spectrum of  $\Delta E$  versus  $E_{\text{total}}$  for  ${}^7\text{Li} + {}^{27}\text{Al}$  at  $E_{\text{lab}} = 9 \text{ MeV}$  and  $\theta_{\text{lab}} = 40^\circ$

## 3.4 Data Analysis

### 3.4.1 Optical Model analysis of elastic scattering angular distribution

Optical model analysis has been carried out to extract the potential parameters using ECIS code [60]. In this analysis Woods-Saxon form of Potential (WSP) was used to extract the optical potential parameters. The measured elastic scattering angular distribution data were normalized to the Rutherford cross sections and plotted as a function of center-of-mass angle ( $\theta_{c.m.}$ ) as shown in the Fig.3.7.

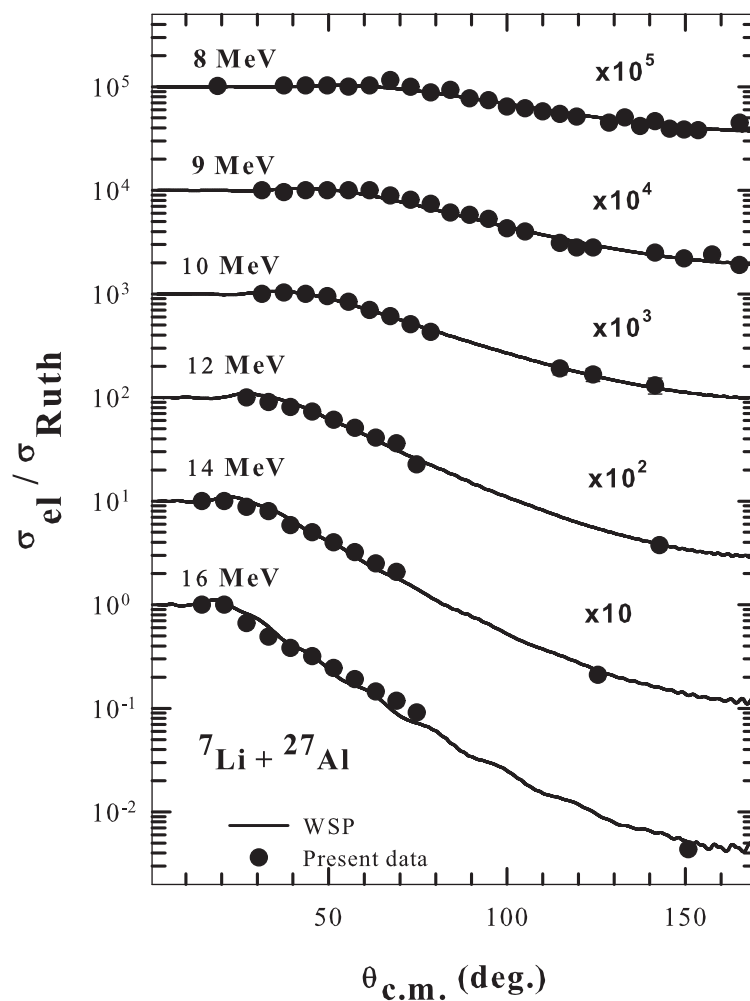


FIGURE 3.7: Elastic scattering angular distributions normalized to the Rutherford cross sections (filled circles) as a function of  $\theta_{c.m.}$  for the  ${}^7\text{Li} + {}^{27}\text{Al}$  system. The Optical Model fit using Woods-Saxon potentials are shown by Solid lines

In order to get the best fit to the experimental data, initially only the real ( $V_o$ ) and imaginary ( $W_o$ ) potential depths have been varied to get the best fit to the experimental data with minimum  $\chi^2$  value. At the same time the reduced radii ( $r_o$ ) and diffuseness ( $a_o$ ) parameters have been kept constant at 1.2 fm and 0.63 fm respectively. Later, the diffuseness parameter has been varied from 0.59 fm to 0.67 fm in steps of 0.02 fm and tuned the potential depth for the best fitting of the experimental data points. This procedure gives many sets of potential parameters which fits the experimental data points equally well with similar  $\chi^2$  value. In order to avoid ambiguities with many sets of potential parameters it is customary to get a radius of sensitivity ( $R_s$ ), where all the potentials carry equal values. The

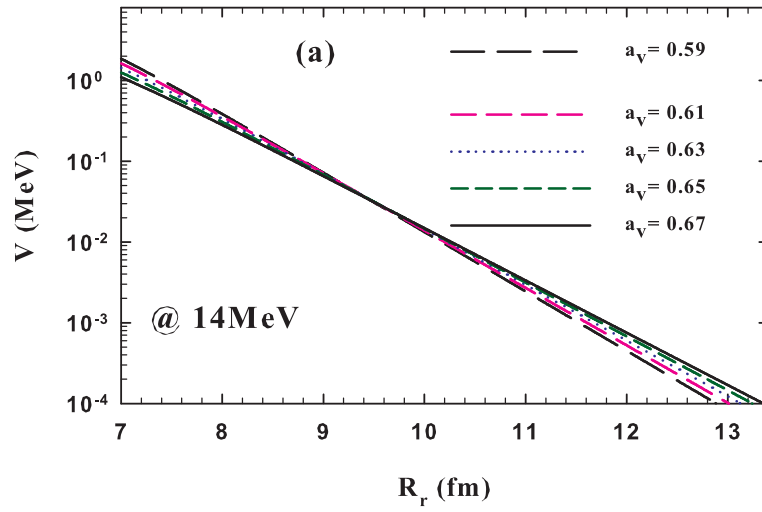


FIGURE 3.8: Radius of sensitivity for real part of the potential at 14 MeV

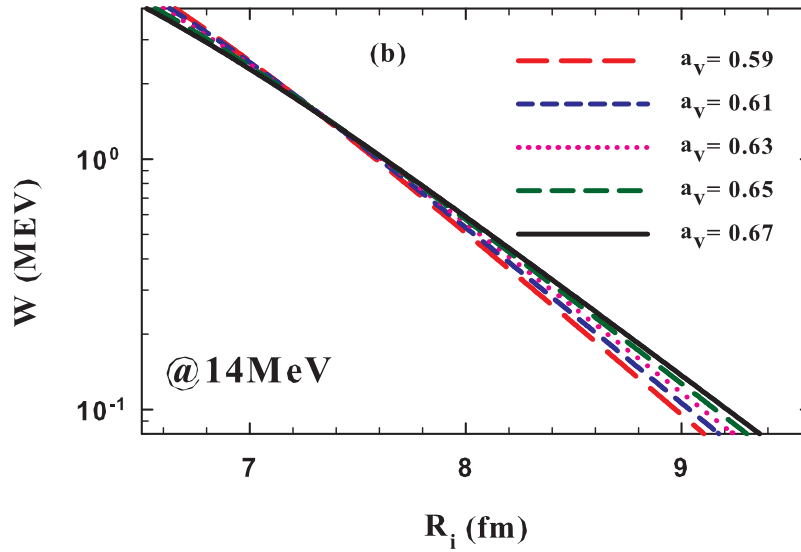


FIGURE 3.9: Radius of sensitivity for imaginary part of the potential at 14 MeV

radius of sensitivity  $R_s$  has been obtained by plotting different potential values as a function of  $r$  (fm) as shown in Fig. 3.8 and Fig. 3.9. From this figure it is observed that all the plots corresponding to different potential parameters intersect at a single value of  $R$ , which has been identified as a radius of sensitivity  $R_s$ . This method was applied to both real as well as imaginary parts of the nuclear potential at all the energies, and an average of  $R_{sr}$  (real part) and  $R_{si}$  (imaginary part) has been considered as a radius of sensitivity ( $R_s$ ), which carries

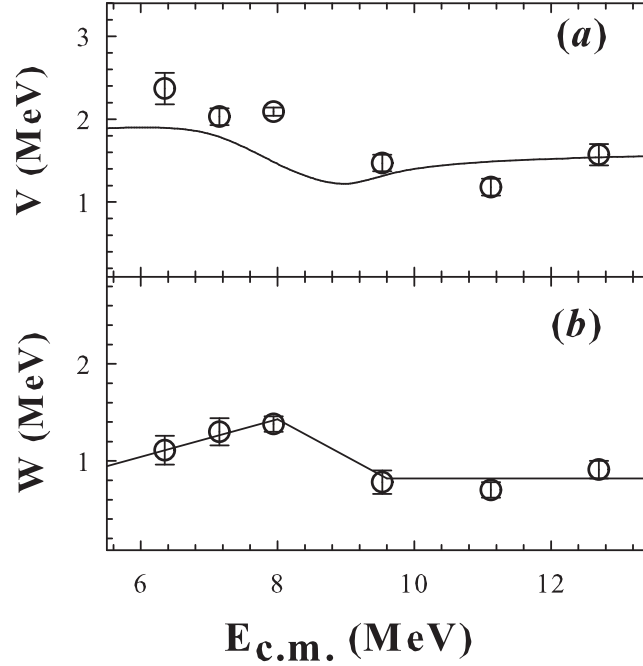


FIGURE 3.10: Energy ( $E_{c.m.}$ ) dependence of the (a) real and (b) imaginary parts of Woods-Saxon potential at  $R_s$  ( $\sim 8.0$  fm) for the  ${}^7\text{Li} + {}^{27}\text{Al}$  system. Dispersion relation calculation is shown by Solid line.

the value of 8.0 fm. From the derived value of radius of sensitivity  $R_s$  (8.0 fm) and mean value of diffuseness parameters  $a_o$  (0.63) the energy dependency of both the real and imaginary potentials have been carried out as shown in Fig. 3.10. The total reaction cross sections and optical potential parameters with a corresponding  $\chi^2/N$  value of the fits, are given in the Table 3.1. It has been observed that the energy dependence of the real and imaginary parts of the Optical Model potential obtained from the present elastic scattering angular distribution data does not show any particular trend of either ‘TA’ or ‘BTA’. Which is in contrast with the observation for the case of  ${}^6\text{Li}$ [30, 31], but consistent with the observation made in the Ref. [61] for the same system.

### 3.4.2 Dispersion relation analysis

In order to check the consistency of the observed energy dependence of the real and imaginary parts ( $V$  and  $W$ ) of the complex optical potential  $U(r, E) =$

TABLE 3.1: Woods-Saxon potential parameters and total reaction cross sections obtained from the Optical Model analysis of the elastic scattering data for the  ${}^7\text{Li} + {}^{27}\text{Al}$  system. The radius and diffuseness parameters were fixed at  $R_r = R_i = 5.90$  fm ( $R_r = R_i = r_0 (A_p^{1/3} + A_t^{1/3})$ ) and  $a_r = a_i = 0.63$  fm.

$E_{lab}$ (MeV)	$E_{c.m.}$ (MeV)	$V$ (MeV)	$W$ (MeV)	$\chi_{min}^2/N$	$\sigma_{reac}$ (mb)
8.0	6.35	61.25	28.61	1.71	289
9.0	7.15	52.54	33.57	1.82	487
10.0	7.94	54.14	35.58	0.45	682
12.0	9.53	37.92	20.09	0.76	869
14.0	11.12	30.57	18.18	0.89	1015
16.0	12.7	40.62	23.61	2.75	1224

$-V(r, E) - iW(r, E)$ , the dispersion relation analysis has been done [44]. The detail of this analysis is given in the Sec2.2.1 (See Chapter 2). In this analysis, the energy dependence of the real potential ( $V$ ) is calculated by assuming the energy dependent imaginary potential to be made of three straight line segments (as shown in the Fig. 3.10(b)). It is seen that the trend of the energy dependence of the real potential is reproduced (as shown by a solid line in the Fig. 3.10(a)). This suggest that both the real and the imaginary parts of the Optical Model potential are consistent.

### 3.4.3 Analysis and discussion of measured $\alpha$ spectra

The  $\alpha$ -particle energy spectra have been measured at five different bombarding energies corresponding to 8, 9, 10, 14 and 16 MeV at backward angles for  ${}^7\text{Li} + {}^{27}\text{Al}$  system. The measured  $\alpha$ -particle spectra can have the contribution from both compound nuclear formation as well as direct reaction channels such as breakup and/or transfer. Also, for a similar light mass system  ${}^7\text{Li} + {}^{28}\text{Si}$  [62], it is verified that the contributions to  $\alpha$ -particle spectra are mostly from the compound reaction channels at backward angles. From the PACE [49] calculations, the possible different  $\alpha$ -particle evaporation channels are shown in Fig. 3.11(a). It has been observed that the combined cross sections of the above  $\alpha$ -particle evaporation

channels constitute  $\sim 32 - 50\%$  of the total fusion cross sections over the measured energy range as demonstrated in the Fig. 3.11(b).

In order to estimate the contributions from direct reactions, the coupled channels calculations using FRESKO (as described in the section 2.6, See Chapter 2) have been performed. The alpha contributions can arise from the projectile breakup ( ${}^7\text{Li} \rightarrow \alpha + t$ ) or transfer followed by breakup channels. The breakup contribution has been obtained from the CDCC calculations. The observed contributions from projectile breakup to measured  $\alpha$ -particles are negligible at backward angles. The other important transfer channels that can contribute to alpha yield is the  $1p$ -pickup by  ${}^7\text{Li}$  to form  ${}^8\text{Be}$ , which in turn can break into two  $\alpha$ -particles. For  ${}^7\text{Li} + {}^{209}\text{Bi}$  reaction [63], it was observed that this channel has a substantial contribution towards alpha production. However, for  ${}^7\text{Li} + {}^{27}\text{Al}$  system, it is observed that the cross sections for the  $1p$ -pickup channel at backward angles are much smaller compared to the evaporation alpha yields.

The measured  $\alpha$ -particle evaporation spectra were obtained in energy bins of 1.0 MeV width. The  $d\sigma_\alpha/d\Omega$  is extracted using the relation given below:

$$\frac{d\sigma_\alpha}{d\Omega} = \frac{d\sigma_{el}}{d\Omega} \times \frac{Y_\alpha}{Y_{el}} \quad (3.2)$$

where  $d\sigma_\alpha/d\Omega$ ,  $Y_\alpha$  and  $d\sigma_{el}/d\Omega$ ,  $Y_{el}$  are the differential cross sections and yields of  $\alpha$ -particle emission and elastic scattering respectively.

### 3.4.4 Statistical model analysis

The Monte Carlo statistical model code PACE [49] has been used to predict the evaporated  $\alpha$ -particle energy spectra. In this calculation the evaporated  $\alpha$ -particle energy spectra were generated by varying magnitude of total fusion cross section ( $\sigma_{fus}$ ) in the PACE input file, such as, to reproduce the measured  $\alpha$ -particle energy spectra. In the PACE code the spin distribution following fusion was parameterized as a Fermi distribution:

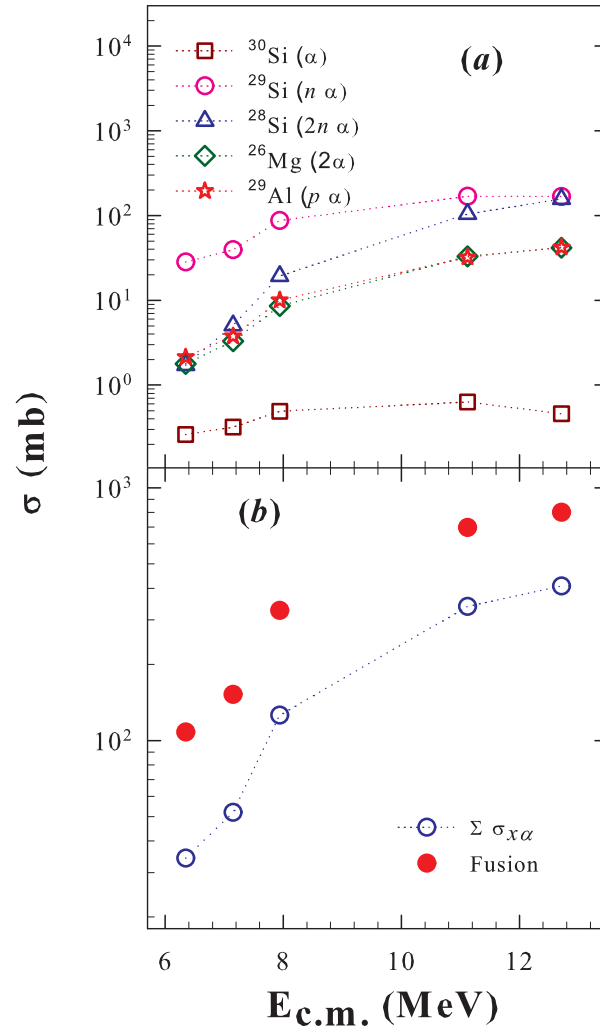


FIGURE 3.11: (a)  $\alpha$ -particle cross sections for different evaporation channels for  ${}^7\text{Li} + {}^{27}\text{Al}$  system from the predictions of PACE code. (b) Comparison of cross sections for the sum of different  $\alpha$ -particle evaporation channels and total fusion cross sections in  ${}^7\text{Li} + {}^{27}\text{Al}$  reaction.

$$\sigma_l = \frac{\frac{\pi}{k^2}(2l+1)}{1 + \exp\left(\frac{l-l_{max}}{\Delta}\right)} \quad (3.3)$$

where,  $\Delta$  is diffuseness parameter,  $k$  is the wave number, and the variable  $l_{max}$  was determined from the relation,  $\sigma_{fus} = \sum_{l=0}^{l_{max}} \sigma_l$ . The level density parameter was set at  $A/10$ . This method was adopted to compare and optimize the  $\alpha$ -particle energy spectra predicted by PACE [49] with the ones from the measurement. Thus, by comparing measured and calculated evaporated  $\alpha$ -particle energy spectra the experimental fusion cross sections have been obtained [64]. Fig. 3.12 shows a

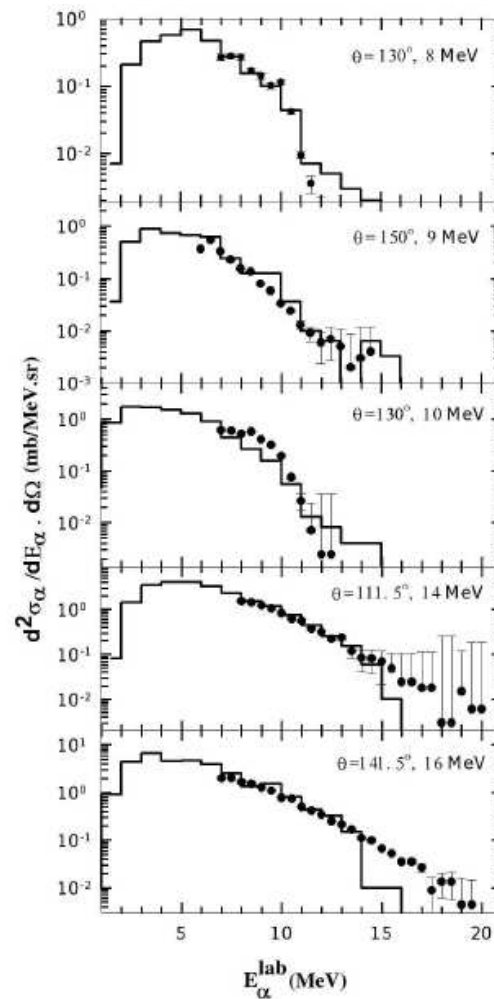


FIGURE 3.12:  $\alpha$ -particle energy spectra measured at various energies in  ${}^7\text{Li} + {}^{27}\text{Al}$  reaction along with the predictions of PACE code. Experimental data points are shown by filled circles and PACE calculations are shown by histograms. All the angles and energies are given in laboratory system.

comparison between measured and PACE predicted  $\alpha$ -particle energy spectra at different angles and bombarding energies. The fusion cross sections obtained at different energies are listed in Table 3.2. In Fig. 3.13 the fusion cross sections ( $\sigma_{fus}$ ) obtained from the present measurements are plotted as a function of energy ( $E_{c.m.}$ ) along with the available literature data.

From this figure, it can be observed that the present fusion cross sections at above barrier energies are in good agreement with the available literature data [34, 35] and at sub barrier energies they are systematically increasing with the energy. The solid line in the Fig. 3.13 shows the predictions of CCFULL code [50], for fusion excitation function with inelastic coupling to target excited state. The coupling of

TABLE 3.2: Fusion cross sections for the  ${}^7\text{Li} + {}^{27}\text{Al}$  system at various bombarding energies extracted from the measured  $\alpha$ -particle spectra.

$E_{lab}$ (MeV)	$E_{cm}$ (MeV)	$\sigma_{fus}$ (mb)
8.0	6.35	$108 \pm 14$
9.0	7.15	$152 \pm 20$
10.0	7.94	$327 \pm 40$
14.0	11.12	$697 \pm 87$
16.0	12.7	$800 \pm 100$

the target inelastic state at 0.842 MeV with deformation parameter  $\beta_2 = 0.31$  has been considered in the calculations. The calculation with no-coupling is not shown in the figure as no much difference was seen in comparison with the calculations that includes inelastic coupling. In the CCFULL calculation the following barrier parameters were used:  $V_b = 6.6$  MeV,  $R_b = 7.97$  fm and  $\hbar\omega = 3.39$  MeV, which gives a reasonable agreement with the present experimental data at near-barrier energies as well as the fusion data available in literature at above-barrier energies. The barrier height that has been used for the above calculations is consistent with the barrier height mentioned in the Ref. [65]. The observed effect from the target inelastic coupling is insignificant in magnitude (similar to the observation made in the Ref.[35]) may be due to low  $Z$  value of the target.

The fusion cross sections in the reactions of different weakly bound projectiles  ${}^6,{}^7\text{Li}$ ,  ${}^9\text{Be}$  with  ${}^{27}\text{Al}$  target are compared in the Fig. 3.14. The data from the present work and Ref. [38] have also been included. It is observed that the present fusion data for  ${}^7\text{Li} + {}^{27}\text{Al}$  reaction at energies around the Coulomb barrier are of the same order as for the  ${}^6\text{Li} + {}^{27}\text{Al}$  system [38].

### 3.4.5 Coupled-Channels Calculations using CDCC and CRC formalism

In order to unfold the effect of couplings of direct reaction channels such as breakup, inelastic and transfer on elastic and fusion cross sections, The Coupled-Channels Calculations using CDCC and CRC formalism, have been carried out

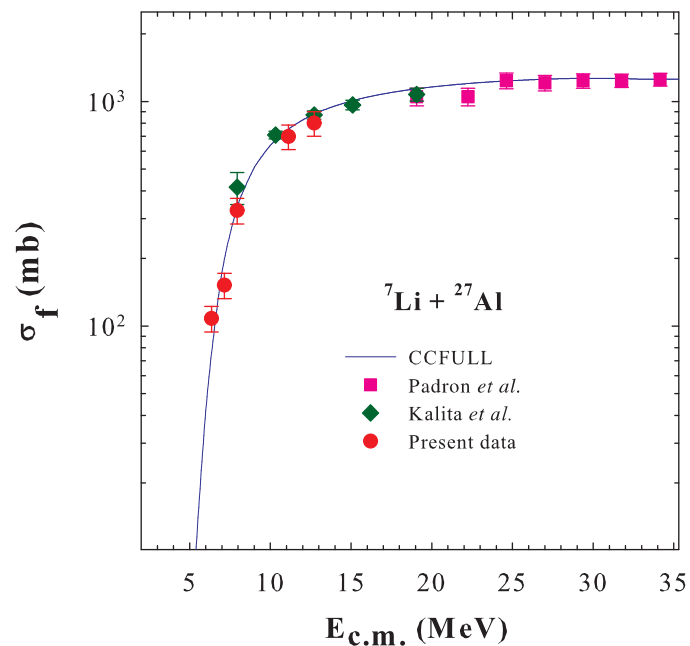


FIGURE 3.13: Fusion cross sections obtained in the present experiment along with the data from the literature and CCFULL predictions for the  ${}^7\text{Li} + {}^{27}\text{Al}$  system. Filled data points represent fusion cross sections from the present measurement. CCFULL calculated fusion cross sections are represented by a solid line. Filled squares and diamonds represent the fusion cross sections from Refs. [34] and [35] respectively.

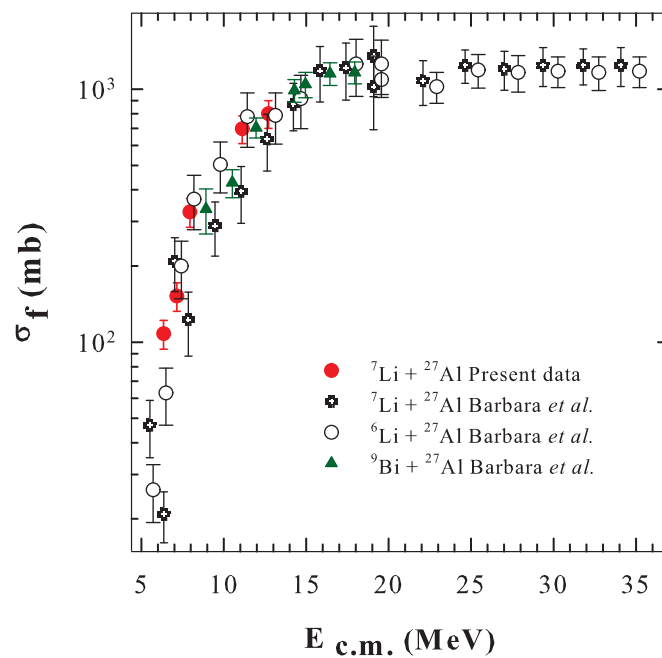


FIGURE 3.14: Comparison of fusion cross sections in the reaction of  ${}^6,{}^7\text{Li}$  and  ${}^9\text{Be}$  with  ${}^{27}\text{Al}$  target at around the Coulomb barrier energies.

using FRESKO code version FRES 2.8.[42]. In this calculation, apart from the projectile breakup, some of the important direct reaction channels are also included. Here, the couplings that are included to study their effects on elastic scattering and fusion reactions are: projectile breakup channels, bound excited state ( $1/2^-$ , 478 keV state) of  ${}^7\text{Li}$  and  $1n$ -stripping transfer channels. In the CDCC calculations the structure of projectile  ${}^7\text{Li}$  has been considered as a cluster of  $\alpha$  and  $t$ , where  $\alpha$  is taken as core and  $t$  is taken as valence particle. The coupling potentials for  $\alpha + {}^{27}\text{Al}$  and  $t + {}^{27}\text{Al}$  have been taken from the Refs. [66, 67] to obtain the cluster folded (CF) potential for the entrance channel. The strength of the real part of the CF potential was needed to be multiplied by a factor of 0.6 to reproduce the measured elastic scattering cross sections at all energies. The continuum of  ${}^7\text{Li}$  ( $\alpha + t$ ) up to the excitation energy of 5 MeV has been considered. This includes the  $1^{st}$  resonant state ( $7/2^-$ , 4.63 MeV) with a width of 0.093 MeV. The non-resonant continuum has been discretized in terms of momentum bins of finite width,  $\Delta k = 0.20 \text{ fm}^{-1}$  and the region around the resonant state has been discretized into much smaller momentum bins ( $\Delta k \sim 0.0050 \text{ fm}^{-1}$ ). The scattering states arising from the combinations of  $\alpha$  and  $t$  have been assumed as excited states of  ${}^7\text{Li}$  with the energy equal to the mean of bin energy range. In the solution of coupled-channels calculations, the scattering wave functions have been integrated up to 80 fm in steps of 0.02 fm and the relative angular momentum up to  $95\hbar$  has been considered.

In the CRC calculations, the coupling to the inelastic scattering corresponding to the projectile ( ${}^7\text{Li}$ ) bound excited state ( $1/2^-$ , 478 keV) and  $1n$ -stripping channel have also been included in the previous CDCC formalism. Coupling of the projectile ( ${}^7\text{Li}$ ) bound excited state is taken similar to the one of the discrete continuum states. Moreover, to study the effect of transfer channels, the dominant  $1n$ -stripping channel i.e.,  ${}^{27}\text{Al}({}^7\text{Li}, {}^6\text{Li}){}^{28}\text{Al}$  was included along with the CDCC calculations. The ground state ( $3^+$ ) and 0.031 MeV ( $2^+$ ) states of  ${}^{28}\text{Al}$  have been included in the calculations. The related spectroscopic factors were taken from the Ref. [68, 69]. The experimental data on elastic, inelastic and transfer channels

act as constraints to the potential and coupling parameters that are used in the FRESCO calculations.

In the Fig. 3.15, the results for the elastic scattering from the above coupled-channels calculations and the present experiment as well as the ones from the literature [61] are compared. The calculations reproduce the elastic scattering data reasonably well over the entire energy range of our measurement. The results of the calculations with no-coupling, only breakup coupling and breakup+transfer couplings are shown by dotted, dashed and solid lines respectively. Interestingly the effect of transfer coupling on elastic scattering particularly at above-barrier energies is significant and more than that of breakup couplings. This can be understood in terms of the reaction probabilities of these two channels as demonstrated in the Fig. 3.16, where the calculated breakup and transfer cross sections are compared as a function of energy. The effect of transfer channel is found dominant in comparison to the breakup at all the energies.

In the Fig. 3.17, the calculated inelastic cross sections (solid lines) are compared with the experimental data (filled circles) that are available in the literature [68] at three energies ( $E_{lab} = 11$  MeV, 14 MeV and 18 MeV). The results shown by solid lines are reasonably close to the experimental data. The results from the neutron transfer calculations are compared with the experimental data (taken from the Ref. [68]) at three different energies as shown in the Fig. 3.18. It is observed that the calculations are in good agreement with the measured experimental data of transfer cross sections corresponding to the g.s. plus  $2^+$  state of the  ${}^{28}\text{Al}$ .

The experimental fusion data and the reaction cross sections derived from the Optical Model analysis of the elastic scattering data in terms of CDCC+transfer calculations, are compared in the Fig. 3.19. Fusion cross section obtained by the barrier penetration model (BPM) option of FRESCO is shown by solid line. The reaction cross sections (dashed line) as well as fusion cross sections (solid line) calculated from FRESCO are very close to the experimental data.

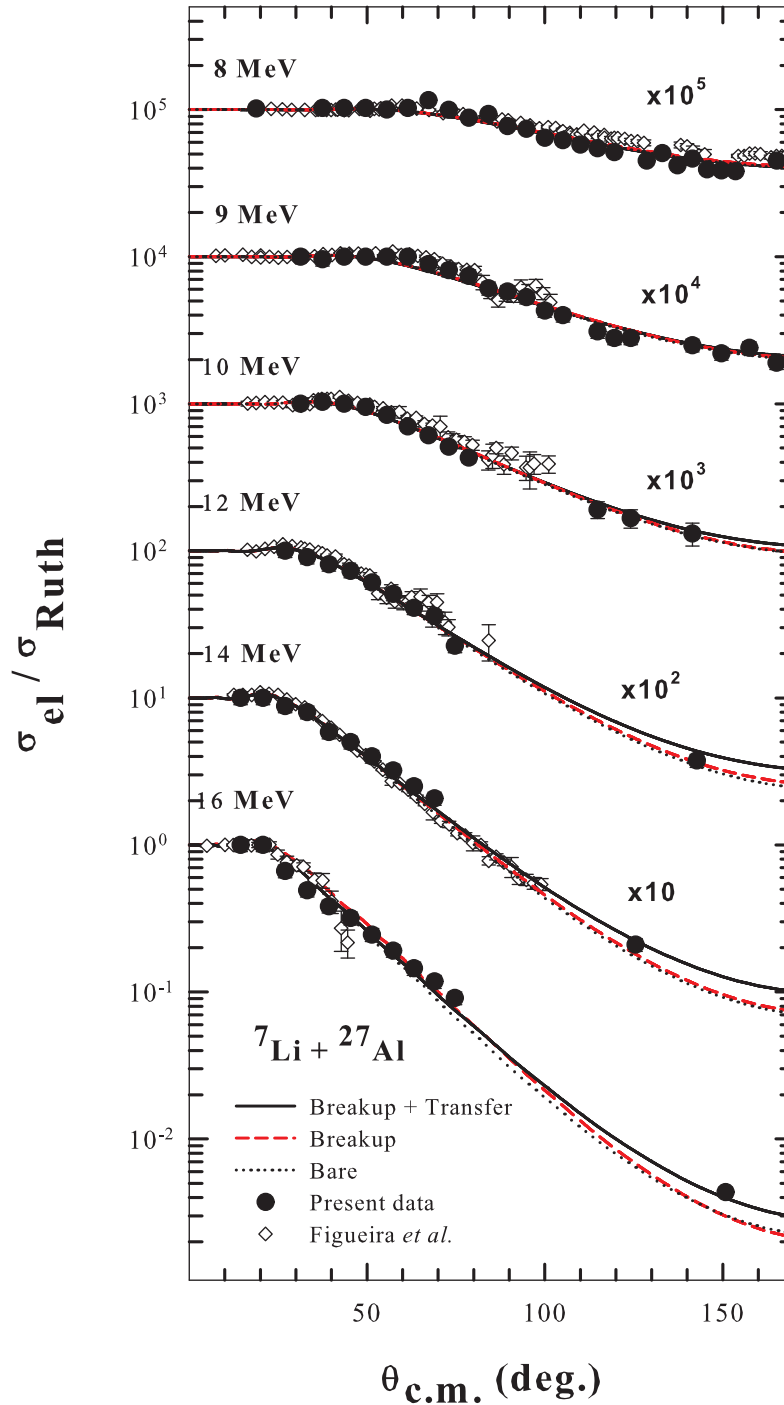


FIGURE 3.15: Elastic scattering cross sections normalized to the Rutherford cross sections as a function of  $\theta_{\text{c.m.}}$  for the  ${}^7\text{Li} + {}^{27}\text{Al}$  system. The filled circles shows the present experimental data points. The open diamonds represent data points from the Ref. [61]. The dotted, dashed (red), and solid (black) lines present the calculations with no coupling, breakup and full (breakup+transfer) couplings respectively.

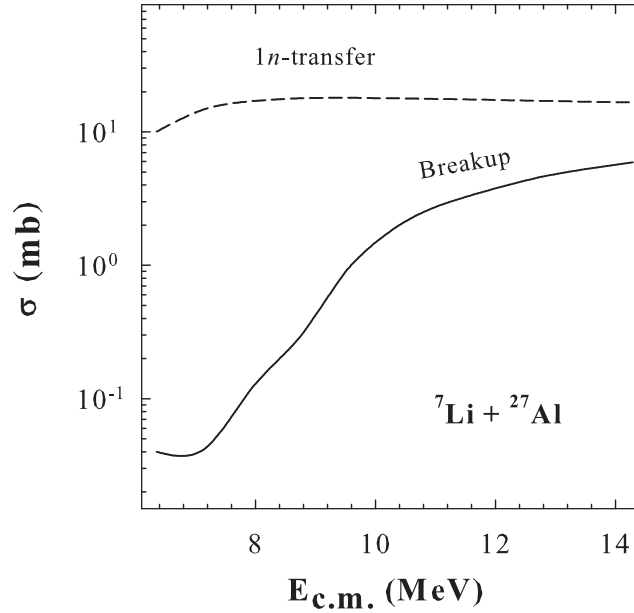


FIGURE 3.16: Breakup and transfer cross sections from the coupled-channels calculations using FRESKO, as a function of  $E_{c.m.}$  in the reaction of  ${}^7\text{Li} + {}^{27}\text{Al}$ .

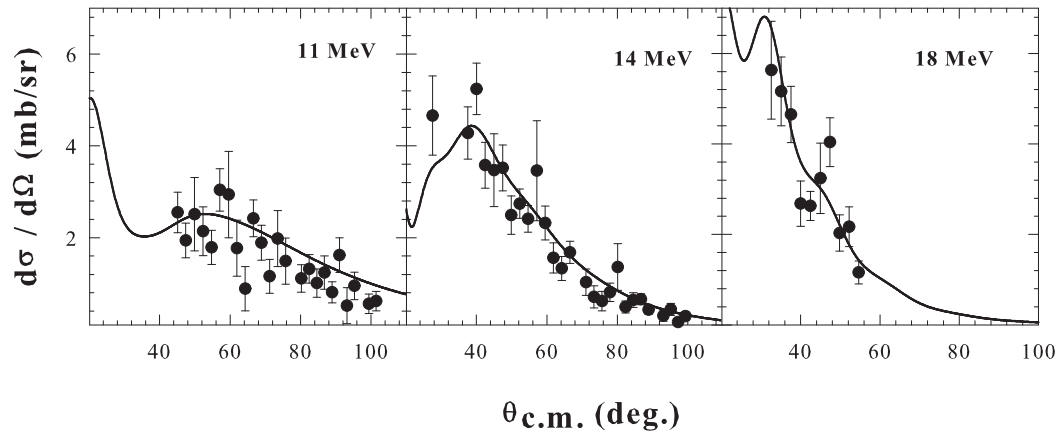


FIGURE 3.17: Inelastic cross sections from the experimental data and the calculations as a function of  $\theta_{c.m.}$  at beam energies of 11, 14 and 18 MeV for  ${}^7\text{Li} + {}^{27}\text{Al}$  system. The filled circles represent the experimental data for inelastic cross sections [68]. The solid line shows the calculated inelastic cross sections that correspond to the bound excited state ( $1/2^-$ , 478 keV) of  ${}^7\text{Li}$ .

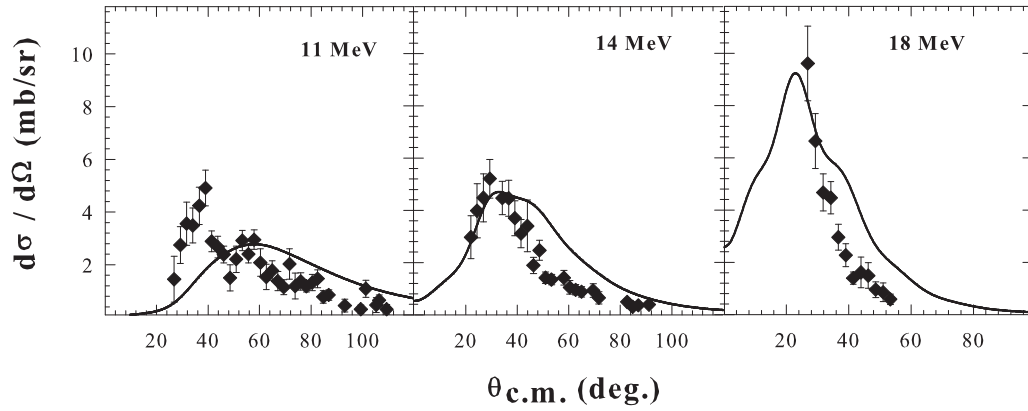


FIGURE 3.18: Transfer cross sections from the experimental data and the calculations as a function of  $\theta_{c.m.}$  at beam energies of 11, 14 and 18 MeV for  ${}^7\text{Li} + {}^{27}\text{Al}$  system. The filled diamonds correspond to the experimental data on transfer cross sections [68]. The solid line represents the sum of the  $1n$ -transfer cross sections corresponding to the g.s. plus  $2^+$  state of the  ${}^{28}\text{Al}$ .

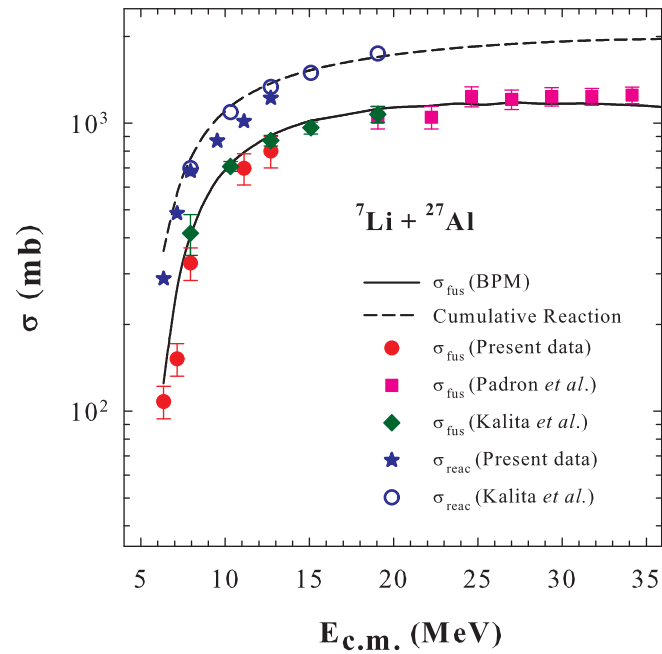


FIGURE 3.19: Comparison of fusion cross sections obtained from the coupled-channels calculations, present measurement (filled circles) and the data from the literature (filled squares) [34] in the reaction of  ${}^7\text{Li}$  with  ${}^{27}\text{Al}$ . The solid and dashed lines represent the BPM fusion and cumulative reaction cross sections respectively obtained from the CDCC calculations with breakup+transfer couplings using FRESKO.

### 3.5 Results and Discussion

In this chapter, elastic scattering angular distribution and fusion cross section measurements have been carried out for the reaction of  ${}^7\text{Li}$  with the light mass target  ${}^{27}\text{Al}$ . The total reaction cross sections ( $\sigma_{Reac.}$ ) and the energy dependence study of the optical potential(WSP) parameters have been done. From the energy dependence of the OM potentials, no strong conclusion regarding the presence of the ‘TA’ or the ‘BTA’ could be made which is consistent with earlier results in the literature. The CDCC and transfer calculations have been carried out to see the breakup and  $1n$ -transfer coupling effects on elastic scattering angular distributions. The  $1n$ -transfer was found to be more dominant as compared to breakup channel particularly at above barrier energies.

Also, the fusion cross sections at energies near the Coulomb barrier were obtained from the measured alpha evaporation spectra at backward angles. The simplified coupled-channels fusion model (CCFULL) calculations can nicely reproduce the present data along and the literature data assuming a fusion barrier height of 6.6 MeV[34]. Fusion cross section for the same target ( ${}^{27}\text{Al}$ ) and three weakly bound stable projectiles ( ${}^6,{}^7\text{Li}$ ,  ${}^9\text{Be}$ ) shows that the present fusion data involving  ${}^7\text{Li}$  is similar to those involving  ${}^6\text{Li}$  [38] around the Coulomb barrier energies, and do not show any suppression compared to the other two reactions ( ${}^6\text{Li}$ ,  ${}^9\text{Be} + {}^{27}\text{Al}$ ), in contradiction to the observation in Ref. [38]. The calculated fusion cross sections from the CDCC+transfer calculations using FRESKO, are also compared with the present fusion data. The obtained fusion cross section by the BPM calculation was found in better agreement with the experimental data.